ACS APPLIED MATERIALS & INTERFACES

Research Article

www.acsami.org

Water Oxidation Catalysis: Effects of Nickel Incorporation on the Structural and Chemical Properties of the α-Fe_2O_3(0001) Surface

Peng Zhao and Bruce E. Koel*

Department of Chemical and Biological Engineering, Princeton University, Princeton, New Jersey 08540, United States

Supporting Information

ABSTRACT: Photoelectrochemical solar fuel synthesis devices based on photoactive hematite (α-Fe_2O_3) anodes have been extensively investigated, yet a fundamental understanding regarding its associated water oxidation surface reaction mechanism is still lacking. To help elucidate detailed reaction mechanisms, we studied water chemisorption and reaction as well as structural changes induced by Ni incorporation into the α-Fe_2O_3(0001) surface. Investigation by scanning probe and electron diffraction techniques show that vapor deposition of Ni and subsequent annealing to 700 K leads to the interdiffusion and incorporation of Ni into the near-surface region of hematite and changes the structure of the (0001) surface by the formation of FeO-like domains on the topmost layer. These results are discussed in the context of a proposed water oxidation mechanism on this surface in which Ni doping facilitates water oxidation by increasing O hole concentrations and forms less negatively charged O anions (*O) and *O···OH species [Liao, P. L.; Keith, J. A.; Carter, E. A. *J. Am. Chem. Soc.* **2012**, *134*, 13296−13309.]. Consistent with predictions from this theory, electrochemical measurements using cyclic voltammetry carried out on the ultrahigh vacuum-prepared surfaces demonstrated that Ni incorporation leads to higher current density and lower onset potential than the unmodified α-Fe_2O_3 surface. Our work utilizing a surface science approach helps to connect such theoretical predictions of reaction thermodynamics on well-defined structures and the performance of modified hematite model electrocatalysts for water oxidation.

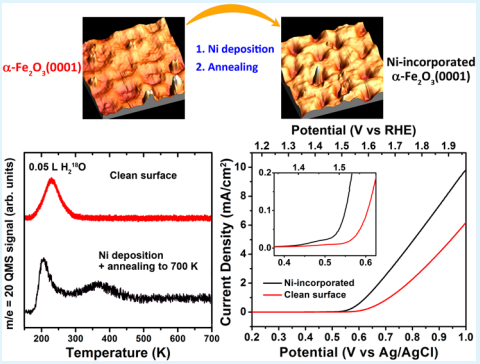

KEYWORDS: *water oxidation, electrocatalysis, surface chemistry, hematite, heterogeneous catalysis*

INTRODUCTION

The nature of the adsorption and reaction of water with transition metal oxide surfaces informs our understanding of the factors influencing the efficiency of the oxygen evolution reaction (OER), a key half-reaction required in various solar fuel production schemes. Hematite (α-Fe_2O_3) has been intensely investigated as an electrode constituent material for this application due to its optimal band gap (2.1−2.2 eV), chemical stability in aqueous nonacidic electrolytes, abundance, and nontoxicity.[1−6] In spite of these advantages, the implementation of α-Fe_2O_3 photoelectrodes has been impeded by several shortcomings, including perhaps most importantly its low associated catalytic efficiency for the OER. This reaction is critically important because the low efficiency of the OER is currently responsible for much of the overall efficiency loss associated with solar-driven hydrogen generation by water splitting. Consequently, researchers actively pursue surface modification with cocatalysts[7] or doping other elements[8−11] as a means to improve reaction kinetics and reduce overpotentials. This pursuit is hampered by the lack of clear knowledge of the active sites and key intermediates responsible for redox reactions as well as on the rate-determining steps in water oxidation reactions.

To investigate these aspects, water adsorption and hydroxylation of hematite surfaces have been studied theoretically by both atomistic simulation[12,13] and density functional theory (DFT).[14,15] Recently, Carter and co-workers have proposed detailed water oxidation mechanism on hematite (0001) surfaces.[16] The reaction pathway intermediates are displayed in a continuous catalytic cycle in Figure 1. The intermediate "*" in structure 1 has one O vacancy in the O-terminated layer. As a result, the positive charge of the Fe atom nearby is reduced. The addition of one water molecule yields $*OH_2$ (structure 2). Next, the surface undergoes two continuous oxidative steps associated with the release of two protons and two electrons. As a result, a hole is located on this deprotonated O anion, making it less negatively charged, denoted as *O. Through this less negatively charged *O, an *OOH product can form by addition of another water and loss of a proton and an electron. Finally, one O_2 molecule leaves the surface along with one proton and one electron.[16]

On the basis of their proposed mechanism, and after consideration of several substitutional surface dopants, Carter and co-workers predicted that a Ni-doped hematite surface yields the most thermodynamically favored reaction pathway. Very recent reports of improved reactivity with Ni doping

Received: September 13, 2014
Accepted: November 25, 2014
Published: November 25, 2014

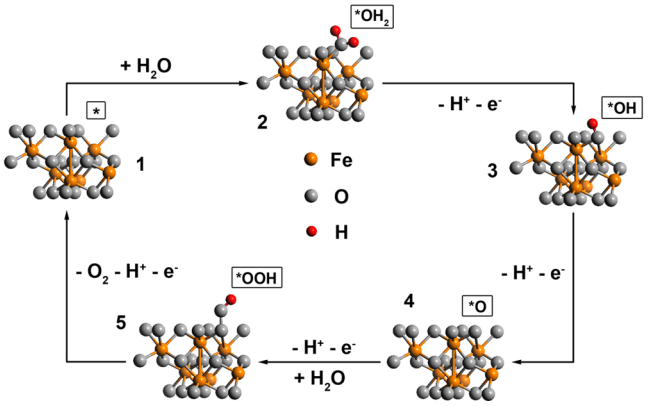

Figure 1. Schematic illustration of the water oxidation reaction pathway on hematite in vacuum according to previous DFT calculations.[16] Reaction intermediates are highlighted with black rectangles. Adapted from Figure 3 of ref 16.

provide initial validations of their prediction.[8,17] Herein, we have combined surface science and electrochemistry approaches to provide additional experimental validation of the theory through the preparation of well-defined hematite surfaces, control of the Ni dopant concentration at the surface, characterization of reactive species at the surface stabilized at low temperatures, and evaluation of the electrochemical performance of these materials for water oxidation. Weiss and co-workers have extensively studied different iron oxide phases and their structure−reactivity correlations.[18−20] On the α-Fe_2O_3(0001) surface at low temperatures in ultrahigh vacuum (UHV), with increasing water exposures, water is first dissociatively adsorbed, followed by molecular chemisorption, and finally condensation in layers of ice. Surface science studies detailing the changes in surface structure and water chemistry by Ni doping of hematite (0001) surfaces have not been reported.

In this article, we report a comparative study of the surface structure, water chemisorption properties, and electrocatalytic activity for water oxidation by thin films of α-Fe_2O_3(0001)/Pt(111) and Ni-incorporated α-Fe_2O_3(0001)/Pt(111). Vapor deposition of Ni and interdiffusion by annealing induces several changes to the α-Fe_2O_3(0001) surface, including the development of FeO-like domains. After Ni incorporation, we observed a new dissociative H_2O adsorption state that desorbs at higher temperature by both temperature-programmed desorption (TPD) and ultraviolet photoelectron spectroscopy (UPS). This new species induced by Ni incorporation is consistent with the effect of Ni doping predicted in ref 16, in which less negatively charged O anions lower the barrier to dissociative water adsorption and enhance the rate of water oxidation. This later prediction was tested directly by cyclic voltammetry (CV) in an electrochemical cell, where we found that the Ni-incorporated surface exhibited enhanced water oxidation activity.

EXPERIMENTAL SECTION

Two multitechnique UHV chambers were used in these studies. The X-ray photoelectron spectroscopy (XPS), Auger electron spectroscopy (AES), low energy electron diffraction (LEED), low energy ion scattering (LEIS), and scanning tunneling microscope (STM) experiments were carried out in a multichamber UHV system with a base pressure of 2.0×10^{-10} Torr. XPS was performed using a PHI 04−548 dual anode X-ray source (Al Kα, 200 W, 15 kV) and a hemispherical analyzer equipped with a five-channel detector (SPECS PHOIBOS 100−5 MCD). LEED was carried out in this chamber using a SPECS 120° rear-view LEED optics. STM experiments were performed with a RHK Technology UHV 300 STM operated in the constant current mode using electrochemically etched tungsten tips with the sample at 300 K. LEIS spectra were carried out using a differentially pumped SPECS IQE-12 ion gun operated at 2.0×10^{-8} Torr to produce a He^+ beam of 1 keV and 0.5 nA sample current incident at 45° with respect to the surface normal. The He pressure in the UHV chamber was less than 1.2×10^{-9} Torr. Sputtering effects from incident He^+ ions is negligible under these conditions. For the qualitative analysis of the LEIS spectrum, the kinetic energy (E_1) of the scattered ion can be calculated according to the single elastic binary collision model from the initial kinetic energy of the ions (E_0), the scattering angle Θ, the mass (M_1) of the scattered ion and the mass (M_2) of the surface atom through the equation:

$$\frac{E_1}{E_0} = \frac{[\cos(\Theta) \pm (A^2 - \sin(\Theta))^{1/2}]^2}{(1 + A)^2}$$

where $A = M_2/M_1$. For the elements under investigation and a He^+ incident beam, the kinetic energy of the scattered ions is 765 eV for Fe and 784 eV for Ni.

The AES, LEED, TPD, and UPS experiments were carried out in a single-level UHV chamber with a base pressure of 2.0×10^{-10} Torr. A PHI 120° LEED optics was used to ensure that the same surfaces were studied in both UHV chambers, in addition to measurements using AES. A double-pass cylindrical mirror analyzer (CMA) was used both for AES and UPS measurements. For UPS measurements, a SPECS helium resonance lamp (He I line 21.2 eV, He II line 40.8 eV) was used with an incident angle of 80° to the sample surface normal. He(II) UPS spectra were taken with the surface normal aligned with the CMA axis for a surface takeoff angle of 42.3° and operating the CMA in constant pass energy mode at 20 eV for a resolution of 0.25 eV.

TPD experiments were performed in this chamber with a heating rate of 3 K/s after gas adsorption at 110 K. All gas exposures given in this paper are in Langmuirs ($1\ L = 1 \times 10^{-6}$ Torr·s) and are uncorrected for ion gauge sensitivity and flux enhancement from a directed tube doser. Water was dosed via leak valves into the UHV chambers. High-purity water was obtained from SigmaAldrich and was degassed prior to dosing by several freeze-pump-thaw cycles.

The Pt(111) surface was cleaned by cycles of Ar^+-ion bombardment at 1 keV (2 μA, 10 min) at 350 K and subsequent annealing in UHV to 1100 K. Onto this surface, Fe or Ni was evaporated by resistively heating a tungsten wire with an iron or nickel wire (ESPI metal, 99.99% pure) wrapped around it. A Fe_3O_4(111) film was prepared as described earlier.[19] The sample was then transferred into a directly connected antechamber and oxidized for 10 min at 1100 K in 10^{-3} Torr O_2. To quench the structure formed under these conditions, the sample was cooled to 300 K in the presence of 10^{-3} Torr O_2. The sample was transferred back into the UHV chamber without further annealing.

The Pt(111) sample holder could be removed from the UHV manipulator and directly attached to a rotating disc electrode (RDE, Pine). For these electrochemical measurements, the crystal was protected by a droplet of pure water (HPLC grade, Fisher) and then immediately transferred from the UHV chamber into an electrochemical cell. During the sample transfer, the UHV chamber and portable glovebag was filled with high purity N_2. The crystal was then immersed in 0.1 M KOH (SigmaAldrich) solution in a three-electrode cell with a Ag/AgCl reference electrode and a platinum wire counter electrode. The distance between crystal and electrolyte was carefully controlled to prevent the side of the crystal from wetting. For the $I-V$ curves, the experiment was performed at a scan rate of 50 mV/s by the potentiostat in a range from 0.0 to +1.0 V versus Ag/AgCl. All the electrocatalysts were stable over 50 CV cycles. All specific activities were calculated using the geometric surface area of the crystal (disk-shaped, 10 mm in diameter and 3 mm thick).

RESULTS AND DISCUSSION

The Clean α-Fe_2O_3(0001) Surface. Because of similar properties of different iron oxides, preparation of thin films of iron oxide in UHV usually is associated with the formation of mixed phases on the α-Fe_2O_3(0001) surface. Previous studies revealed the α-Fe_2O_3(0001) surface structure greatly depends on the experimental conditions, especially oxygen pressure.[18,19,21,22] Weiss and co-workers,[19] prepared a Fe_3O_4(111) film, which was then oxidized in 1 mbar O_2. The single-phase film surface was almost covered by an oxygen-terminated structure. As the O_2 pressure decreases from 10^{-1} to 10^{-5} mbar, oxygen-terminated surface areas decrease and the coexisting iron-terminated surface areas increase. The lateral size of these domains decreases from values of 200−900 Å to 10−20 Å. Although the surface contains both O- and Fe-terminations, it is still single-phase α-Fe_2O_3. A biphase structure with coexisting α-Fe_2O_3(0001) and FeO(111) islands was observed by Thornton and co-workers,[22] who prepared an α-Fe_2O_3(0001) surface by a final oxidation at 1100 K in 10^{-6} Torr O_2. The phases form a triangular superstructure, which can be explained in terms of the lattice mismatch between two types of oxygen sublayers. In our work reported herein, based on these results, we performed a final oxidation of the Fe_3O_4(111) film at 1100 K in 1×10^{-3} Torr O_2 to obtain the single-phase hexagonal α-Fe_2O_3(0001) surface.

As shown in Figure 2a, this film exhibits a LEED pattern that corresponds to a single-phase hexagonal surface unit cell with a lattice constant of 5 Å. There is no Moiré pattern that would suggest the presence of an Fe_2O_3−FeO biphase film. The surface was further investigated by STM to rule out the possibility of a biphase structure.

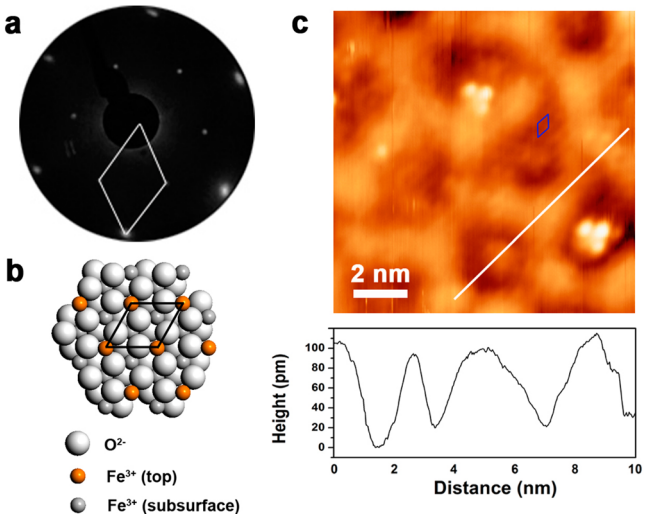

Figure 2. (a) LEED pattern of α-Fe_2O_3(0001) surface (at 60 eV). (b) Top view of the α-Fe_2O_3(0001) surface. (c) STM image of the clean α-Fe_2O_3(0001) surface. The light patches are attributed to oxygen-terminated surface structures, while the dark patches are attributed to an iron-terminated surface possessing a hexagonal surface lattice with the indicated unit cell 5 Å in size (blue cell). Below the image is a line profile along the white line superimposed on the STM image. (image: 11 nm × 11 nm; +2.9 V, 0.3 nA).

Figure 2c shows an STM image in which a hexagonal lattice with 5 Å periodicity can be seen within dark patches. According to the literature on the structure of different iron oxides,[18] 5 Å periodicity is characteristic of the α-Fe_2O_3(0001) surfaces terminated by Fe layers. Although no atomic resolution STM images of the light patches were obtained, line profiles were used to investigate the surface termination further. Along different directions (line profile in Figure 2c), the light domains are 0.75−0.85 Å higher than dark domains. Considering the interlayer spacing of Fe−Fe in α-Fe_2O_3(0001) (0.59 Å), Fe−O in α-Fe_2O_3(0001) (0.85 Å) and Fe−O in FeO(111) (1.25 Å), the light domains should correspond to α-Fe_2O_3(0001) surfaces terminated by an O layer. Supporting Information, Figure S7 shows the structure of the clean α-Fe_2O_3(0001) surface at a larger scale. Thus, we assign the prepared surface as a single phase consisting of α-Fe_2O_3(0001) with regions of Fe and O terminations.

H_2O Adsorption on the Clean α-Fe_2O_3(0001) Surface. Figure 3 shows TPD spectra of water adsorbed on clean α-Fe_2O_3(0001), as well as the corresponding TPD peak area plot. On the α-Fe_2O_3(0001) surface, a chemisorbed species, α, is observed at the lowest exposures in Figure 3a. The desorption peak maximum shifts from 250 to 210 K as the exposure increases to 0.06 L. Another species, β, desorbs initially in a peak at 190 K when the exposure is larger than 0.06 L. With increasing coverage, the desorption peak maximum shifts to slightly lower temperature (180 K at 0.2 L) before condensation (γ species) begins. Condensation is identified by the common leading edge of the desorption traces at higher exposures, characteristic of zero-order kinetics. The total TPD peak area data forms a straight line (inverted triangles) as a function of exposure, which passes through the origin (Figure 3b), indicating a constant sticking probability for water on α-Fe_2O_3(0001) at 110 K. We utilized a cutoff temperature of 200 K as an attempt to distinguish between α species and β species. The curve (triangles) for the component above 200 K becomes constant for water exposures above 0.06 L, which indicates the saturation of α species after 0.06 L in Figure 3a. At higher exposures, the curve (circles) for the 165−200 K component starts to rise after 0.06 L, and saturates at ∼0.2 L. We regarded 165 K as a cutoff between the β and γ species. The 125−165 K curve (squares) has a similar slope as the total peak area curve and arises only after the 165−200 K curve becomes constant at 0.2 L. The shift of the desorption peaks of the α species toward lower temperatures are typically attributed to repulsive adsorbate−adsorbate interactions, but we assign this to second-order desorption kinetics. This would be consistent with the observation of dissociatively adsorbed water in UPS spectra presented below.

He(II) UPS spectra following an exposure of 10 L H_2O on α-Fe_2O_3(0001) at 125 K and after heating this adsorbed layer to increasing temperatures are shown in Figure 4. Since the molecular orbital structure is different for H_2O(a) and OH(a), UPS can be used to discriminate between these species. To better distinguish the UPS peaks arising from adsorbed species, difference spectra (Figure 4b) were obtained by subtracting the spectrum of the clean surface from the spectra for the adsorbate-covered surface. Vertical bars at the bottom of Figure 4b provide the peak positions of gas-phase H_2O. The spectrum at 125 K after condensation of a film of ice (γ) shows the typical three-peak structure of molecular H_2O that arises from emission the $1b_1$ (5.3 eV), $3a_1$ (8.0 eV), and $1b_2$ (11.3 eV) molecular orbitals. When the sample is heated to 155 K, the intensities of these peaks undergo decreases, and the whole spectrum also shifts to lower binding energy. We can still recognize the three peaks at $1b_1$ (5.0 eV), $3a_1$ (7.4 eV), and $1b_2$ (11.1 eV), if we amplify the spectrum. This species is

dx.doi.org/10.1021/am5062773 | ACS Appl. Mater. Interfaces 2014, 6, 22289−22296

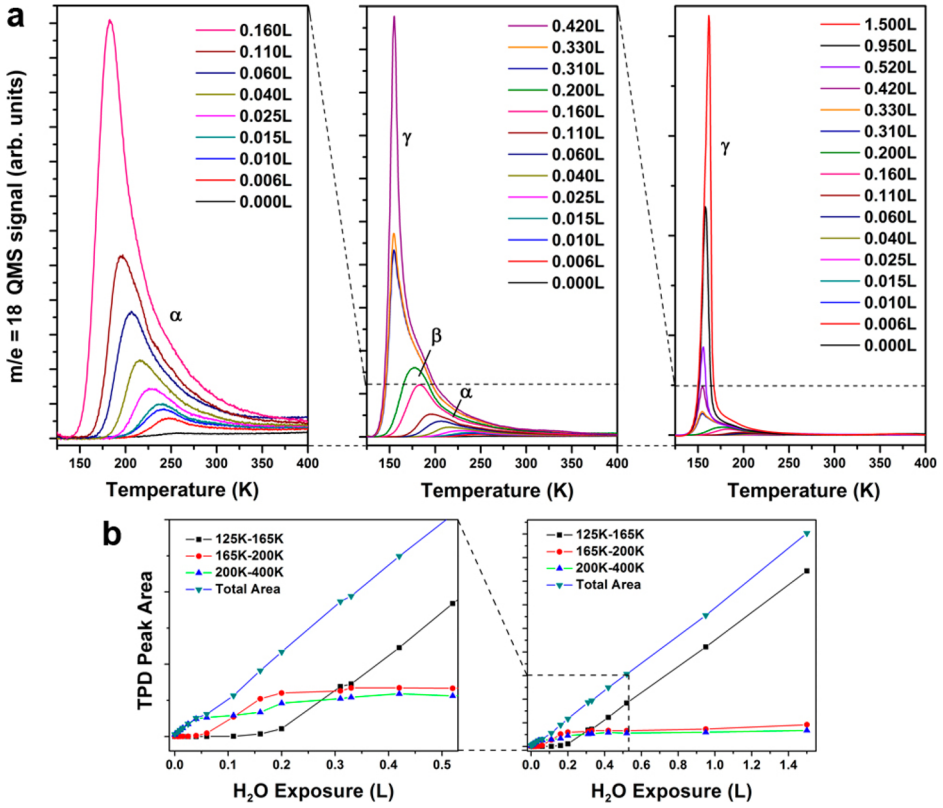

Figure 3. (a) H_2O TPD spectra (m/e = 18) after adsorption of H_2O onto α-Fe_2O_3(0001) at 110 K and different exposures (in Langmuirs). Spectra on the left are enlarged parts of the spectra on the right. (b) H_2O uptake curves showing plots of the total TPD peak area (inverted triangles), area of the desorption peak above 200 K (triangles), area of the peak between 165−200 K (circles), and area of the peak between 125−165 K (squares).

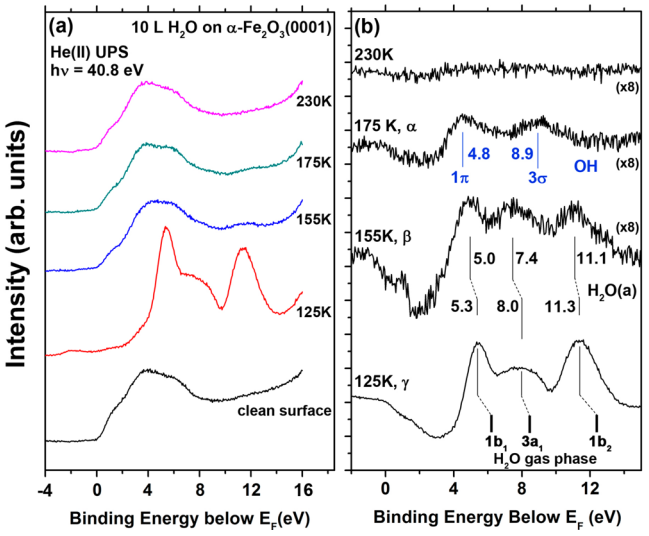

Figure 4. (a) Warm-up series from He(II) UPS spectra after exposure of H_2O on α-Fe_2O_3(0001) at 125 K. All spectra were obtained after heating to and holding at the indicated temperatures. (b) Difference spectra obtained by subtracting the spectrum of the clean surface from the respective adsorbate-covered spectrum in (a). The $1b_1$, $3a_1$, and $1b_2$ energy levels of molecular water and the 3σ and 1π levels of surface-bound hydroxyl groups are indicated. The energy levels for gas-phase H_2O are also provided at the bottom.

interpreted as molecular water[23] and corresponds to species β in Figure 3. The features between 0 and 4 eV below the Fermi level (E_F) are ascribed to adsorbate-induced changes in the substrate emission, which cannot be separated from the water-induced emission. The next spectrum above 175 K consists of two main broad peaks at 4.8 and 8.9 eV attributed to OH(a) species resulting from dissociation of water. The two peaks are due to the 1π and 3σ orbitals of OH(a) as assigned previously for OH(a) on other metal oxides.[24]

Incorporation of Ni into α-Fe_2O_3(0001). As a first step of synthesizing a Ni-incorporated surface film at the α-Fe_2O_3(0001) surface, we deposited less than one monolayer (ML) of Ni on the α-Fe_2O_3(0001) surface at 300 K. We then heated the crystal at 700 K for 15 s in vacuum. XPS and low energy ion scattering (LEIS) were used to characterize these surfaces. All spectra were obtained with the sample at 300 K, including those after heating. Ni 2p XPS spectra in Figure 5b show that, while Ni deposition forms metallic Ni(0), likely in clusters, there is no Ni(0) peak and only a Ni(II) peak after annealing to 700 K. The binding energy of the $2p_{3/2}$ peak for Ni(III) or Ni(IV) is between 856 and 857 eV,[25] which was not observed as shown in Figure 5b. LEIS measurements, which only detect signals from the outermost atomic layer at the surface, as shown in Figure 5c, indicate that, while there is Ni in the topmost layer after Ni deposition, it is no longer observed after annealing to 700 K. Since the probing depth of XPS is up to 1.0 nm (Ni 2p signal) and 1.2 nm (Fe 2p signal), these data indicate Ni exists as Ni(II) in the near-subsurface region. We also carried out depth profile measurements utilizing Ar^+ ion sputtering monitored by LEIS and XPS, as shown in Supporting Information, Figure S2. Both techniques show that the concentration of Ni is 10−15 atom % at a depth of 0.6 nm and decreases with increasing sputtering deeper into the bulk. No Ni was detected beyond ∼2.0 nm deep in the hematite subsurface region. In summary, the 700 K annealing

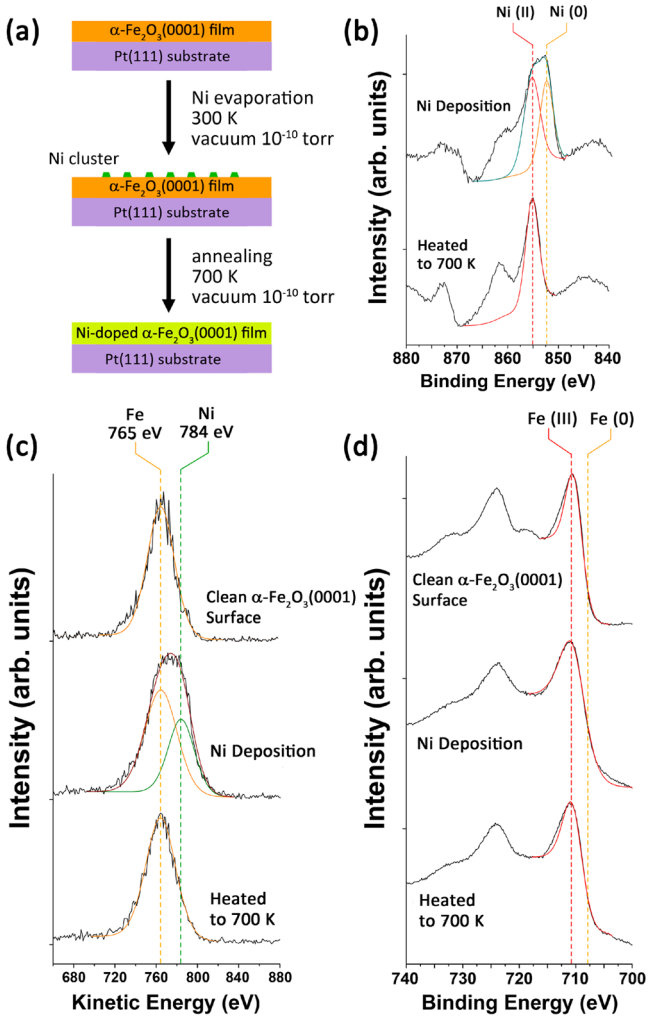

Figure 5. (a) Schematic representation of Ni cluster growth on an α-$Fe_2O_3(0001)$ surface at 300 K and subsequent diffusion into the subsurface region when heated to 700 K. (b) Ni 2p XPS spectra after Ni deposition on α-$Fe_2O_3(0001)$ surface at 300 K and after subsequent heating to 700 K. (c) LEIS spectra of an α-$Fe_2O_3(0001)$ surface before Ni deposition, after Ni deposition at 300 K, and after subsequent heating to 700 K. (d) Fe 2p XPS spectra of an α-$Fe_2O_3(0001)$ surface before Ni deposition, after Ni deposition at 300 K, and after subsequent heating to 700 K.

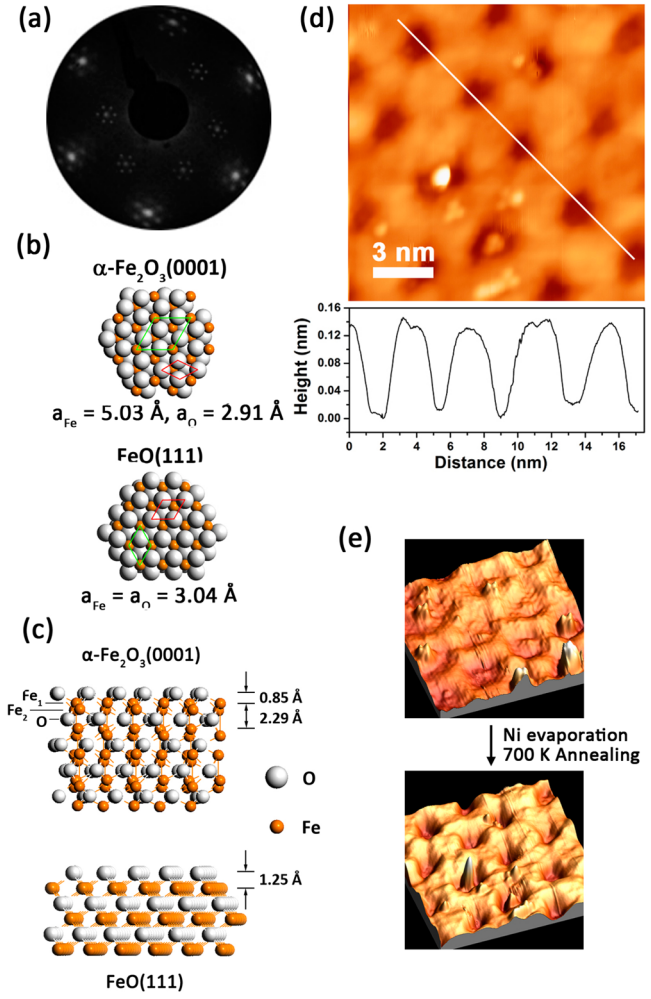

Figure 6. (a) LEED pattern (beam energy of 60 eV). (b) Top view of α-$Fe_2O_3(0001)$ and FeO(111) surfaces. (c) Side view of α-$Fe_2O_3(0001)$ and FeO(111) surfaces. (d) STM image of the Ni-incorporated surface formed by Ni deposition on α-$Fe_2O_3(0001)$ at 300 K and then annealing to 700 K. Below the image is a line profile along the white line superimposed on the STM image. (image: 15 nm × 15 nm; +2.9 V, 0.3 nA) (e) 3D STM topographic images of the clean α-$Fe_2O_3(0001)$ surface in Figure 2 and the Ni-incorporated α-$Fe_2O_3(0001)$ surface.

treatment leads to the interdiffusion and incorporation of Ni into a near-surface film of α-$Fe_2O_3(0001)$.

The 700 K annealed surface was also examined with LEED (Figure 6a), revealing a pattern in which the primary beams have the same spot distances as the clean α-$Fe_2O_3(0001)$ LEED pattern but with each LEED beam surrounded by smaller satellite spots having hexagonal symmetry. This type of α-$Fe_2O_3(0001)$ LEED pattern has been reported,[22,26,27] and is explained by a Moiré pattern on the basis of multiple scattering across interfaces.[28] Structural models of α-$Fe_2O_3(0001)$ and FeO(111) surfaces are shown in Figure 6b.[21] The O layer of the α-$Fe_2O_3(0001)$ surface has a hexagonal lattice with a periodicity of 2.91 Å, while the Fe layer has a hexagonal lattice with a periodicity of 5.03 Å. The structure of FeO(111) single-crystal surface is quite different; that is, both of the O and Fe terminations show hexagonal lattices with the same periodicity of 3.04 Å. LEED observations of the surface of the Ni-treated α-$Fe_2O_3(0001)$ film can be ascribed to formation and resulting lattice mismatch of a thin FeO(111) adlayer or adislands on the α-$Fe_2O_3(0001)$ surface.

STM images (Figure 6d) reveal additional structural details about the Ni-incorporated surface. After treatment the holes (dark domains) are smaller, and the islands (light domains) are larger. There is no light patch at the center surrounded by dark patches, as for the clean surface. In a line profile from the STM image, as shown in Figure 6d, holes on the modified α-$Fe_2O_3(0001)$ surface (after annealing) are much deeper than those on the clean α-$Fe_2O_3(0001)$ surface. Light domains are 1.2−1.3 Å higher than dark domains, which corresponds to the interspacing between Fe and O layers in FeO(111) (1.25 Å) (Figure 6c). These changes are also clearly seen in a direct comparison of the respective three-dimensional (3D) STM topographic images (Figure 6e). Supporting Information, Figure S7 shows the structure of the Ni-incorporated α-$Fe_2O_3(0001)$ surface at a larger scale. We attribute the very small changes in the Fe 2p XPS peaks in Figure 5d to the small chemical shift and small relative intensity of FeO compared to

dx.doi.org/10.1021/am5062773 | ACS Appl. Mater. Interfaces 2014, 6, 22289−22296

Fe_2O_3. According to LEIS all Ni atoms diffuse into the subsurface region and are identified as Ni^{2+} in XPS, while most of the Fe atoms are observed in the 3+ oxidation state throughout the XPS probing range. These results are consistent with formation of a thin film of Ni-incorporated α-Fe_2O_3, with a large portion of the topmost surface layer comprised of a single layer of O-terminated FeO(111) domains.

Such changes in the hematite surface structure have not been reported before. Reoxidation of the surface was attempted by annealing the Ni-treated sample at 700 K in 10^{-3} Torr of O_2 for several minutes, but there was no change in the structure of the surface as probed by XPS, LEIS, STM, and LEED. We also characterized the structure of α-Fe_2O_3(0001) surface with no Ni after heating at 700 K in vacuum and the surface annealed at 700 K after water adsorption to check if FeO is formed by annealing α-Fe_2O_3(0001) surface at higher temperature, instead of Ni incorporation. There was no change in the structure of the surface as probed by STM, XPS, and TPD, as shown in Figures S3–S5 in Supporting Information.

H_2O Adsorption on the Ni-Incorporated α-Fe_2O_3(0001) Surface. Water adsorption and desorption on the Ni-incorporated α-Fe_2O_3(0001) surface (Ni deposition at 300 K and annealing to 700 K), characterized in the previous section, was studied by TPD and UPS. The surface was exposed to 0.05 L $H_2{}^{18}O$ at 150 K. Figure 7a shows dissociatively chemisorbed species that desorb water at 200–250 K (α_1) on the clean surface, which is consistent with the 0.040 L curve in Figure 3a. It is obvious from a comparison of the TPD traces in Figure 7a,b that the Ni-incorporated surface is more reactive to water than the clean α-Fe_2O_3(0001) surface. The amount of water desorbed at temperatures above 200 K, which is indicative of recombination of dissociated water, is about 20% larger. More interesting, in addition to a somewhat narrower α_1 peak there is a second (α_2) peak at a higher desorption temperature; that is, another species (α_2) is still present at temperatures up to 450 K. To establish that the surface is stable to water adsorption and desorption, Figure 7b shows three successive TPD experiments in which H_2O adsorption and subsequent heating to 700 K occurred. This caused no change in the TPD plots up to 700 K.

To prove that the surface chemistry after Ni incorporation is different from FeO(111) surfaces, H_2O TPD experiments were also carried out on surfaces of separately grown FeO(111) films on a Pt(111) substrate (Figure S1 in Supporting Information). On FeO(111), a physisorbed species desorbs initially in a peak at 180 K. After increasing coverage above 0.35 L, condensation begins. The absence of water TPD peaks due to dissociative adsorption on FeO(111), but not on the modified α-Fe_2O_3(0001) surface, indicates a specific chemical interaction induced by Ni incorporation and surface structural changes.

UPS spectra taken after an exposure of 10 L H_2O on the Ni-incorporated surface at 125 K, as shown in Figure 8, show the same valence-band features observed in Figure 4 for the condensed H_2O film. When the sample was heated to 155 K, these peaks shifted to lower binding energy. All condensed ice species are desorbed, and so the spectrum corresponds to primarily molecularly chemisorbed H_2O species (β). According to TPD experiments (Figure 7), species that ultimately give rise to both α_1 and α_2 peaks are on the surface at 180 K. Only species that give rise to the α_2 peak in TPD still exist on the surface at 240 K. In the UPS difference spectra, the OH valence-band features, consisting of two main peaks at 5.2 and 8.0 eV, appear after heating to 180 K. These are attributed to

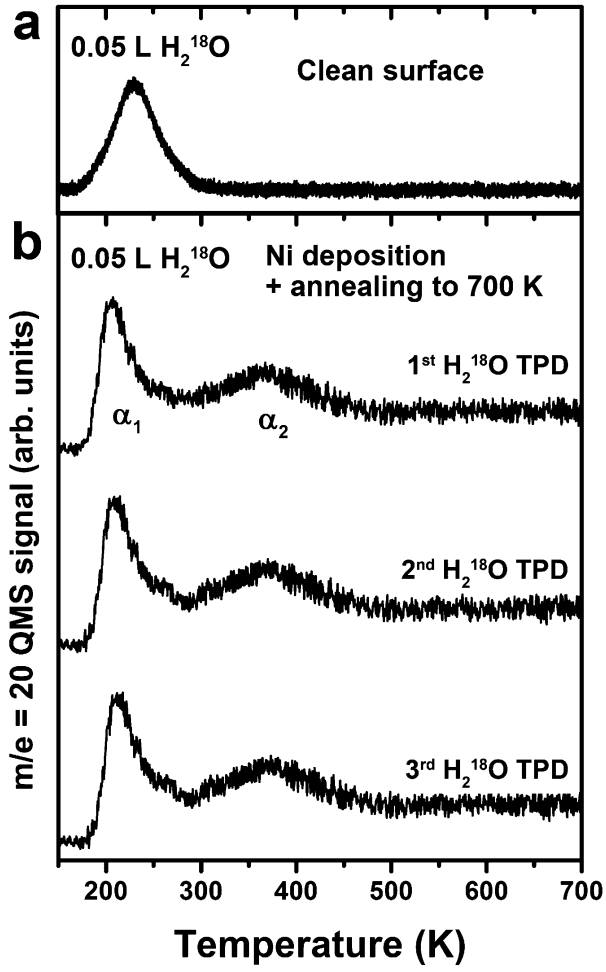

Figure 7. $H_2{}^{18}O$ TPD spectra (m/e = 20) after exposure of 0.05 L $H_2{}^{18}O$ onto a α-$Fe_2{}^{16}O3$(0001) surface at 150 K (a) without Ni deposition and (b) with Ni deposition followed by heating to 700 K. Three identical TPD experiments were carried out successively to explore the stability of the surface after H_2O adsorption and heating to 700 K.

the 1π and 3σ orbitals of adsorbed OH species. Further annealing to 240 K causes a small shift of these two peaks. Thus, the species that appear in the UPS spectra at 180 K, which give rise to α_1, and those species in the spectra at 240 K, which give rise to α_2, are very similar and both are derived from surface-bound OH groups (Figure 8). Importantly, the species responsible for the α_2 desorption peak can still be formed after several cycles of H_2O TPD experiments that entail heating to 700 K (Figure 7b), which indicates that the composition and structure of the Ni-incorporated surface is thermally stable under these conditions.

Coordinatively unsaturated oxygen atoms can play an important role in adsorption on oxides. Like defects, coordinatively unsaturated oxygen atoms make many surfaces more reactive toward water decomposition and hydroxylation. Carley et al.[29] have reported that the Ni(210) surface preoxidized at 77 K possesses very high activity in dissociating water molecules to hydroxyl groups. The O 1s XPS spectrum was similar to that for β-NiO·OH, which has three components assigned to oxide (O^{2-}), hydroxide, and water, the water being intercalated within the nickel oxide lattice. They claimed that the oxygen species in the surface oxide layer that were active toward water dissociation were those that are less negatively

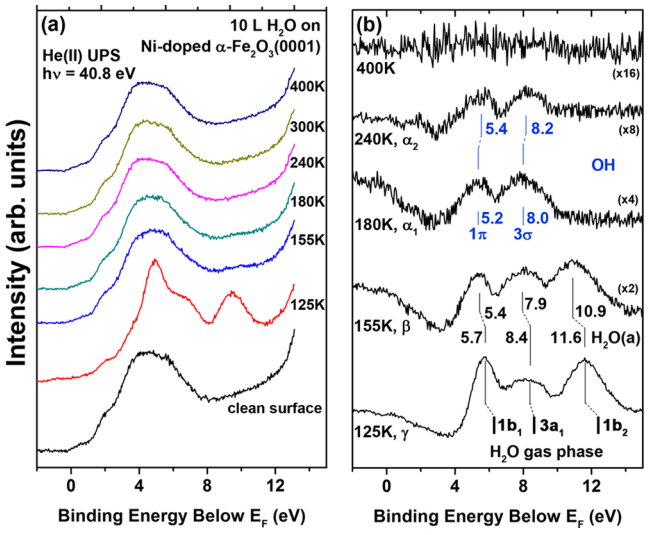

Figure 8. (a) Warm-up series from He(II) UPS spectra after exposure of H_2O on Ni-incorporated α-Fe_2O_3(0001) at 125 K. All spectra were obtained after heating to and holding at the indicated temperatures. (b) Difference spectra obtained by subtracting the spectrum of the clean surface from the respective adsorbate-covered spectrum in (a). The $1b_1$, $3a_1$, and $1b_2$ energy levels of molecular water and the 3σ and 1π levels of hydroxyl groups are indicated. The energy levels for gas-phase H_2O are also provided at the bottom.

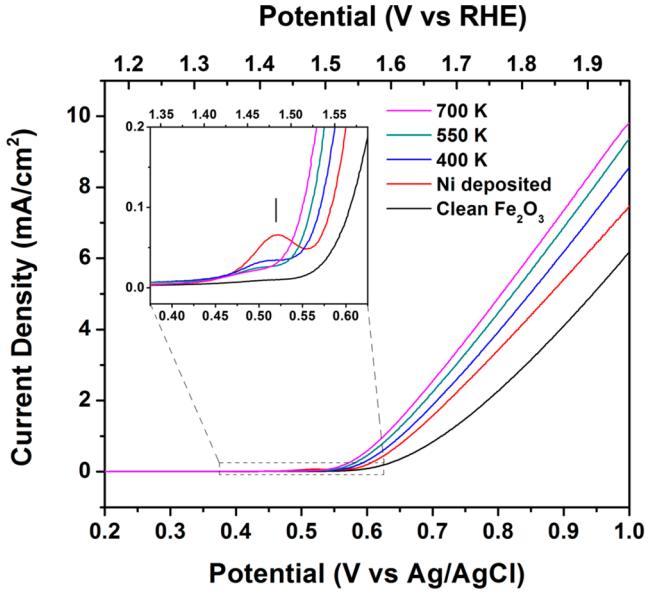

Figure 9. Current–potential plots in the dark for α-Fe_2O_3(0001) surfaces before Ni deposition, after Ni deposition at 300 K, and then after subsequent heating to 400, 550, and 700 K. These measurements were made in 0.1 M KOH with a sweep rate of 50 mV/s. The inset shows magnification of the region where the onset potential occurs, and the vertical line indicates the peak likely due to Ni oxidation. Only anodic scans are shown here.

charged, coordinatively unsaturated, and accessible to adsorbed water molecules. Norton et al.[30] also suggested that the reason for differences in reactivity for water oxidation following different oxygen treatments was due to differences in the degree of coordinative unsaturation between the various types of oxygen.

Liao et al.[16] concluded that when less positively charged Ni dopants are introduced into the Fe_2O_3 lattice in the subsurface region, diffusion of electrons from the bulk is suppressed, suggesting probable hole localization on O anions (to form *O anions) on the surface. Unlike the typical FeO(111) surface, which only weakly physisorbs molecular H_2O, the FeO-like surface *O anions generated from Ni-doping are more likely to be involved in the water oxidation cycle than O anions on the clean α-Fe_2O_3(0001) surface. This is because they can act as "nonlattice" oxygen atoms and produce coordinatively unsaturated oxygen sites. Hole localization on less negatively charged *O anions makes it easier for H_2O molecules to dissociatively bind with Fe atoms nearby, since the hydroxyl groups from dissociation can form an *O···OH bond with the less negatively charged *O anion.

Electrochemical Measurements. The activity of the Ni-incorporated α-Fe_2O_3(0001) surface for water oxidation was compared to that of the clean surface in 0.1 M KOH solution by cyclic voltammetry. Figure 9 shows current density–potential curves for α-Fe_2O_3(0001) surface before Ni deposition, after Ni deposition at 300 K, and then after further annealing to 400, 550, and 700 K. After deposition of Ni without annealing, an enhancement in the current for water oxidation was observed, reaching 3.4 mA/cm^2 at a potential of 0.80 $V_{Ag/AgCl}$, compared with 2.3 mA/cm^2 on the Ni-free α-Fe_2O_3(0001) surface. In the enlarged onset region where the current starts to rise (Figure 9 inset), another peak was observed for the Ni-deposited surface (assigned by vertical line). This might be due to the oxidation of Ni clusters on the surface. As the Ni-deposited surface is heated to higher temperature, this peak associated with Ni oxidation drops and eventually disappears at 700 K, which is consistent with the structural changes proposed above as probed by LEIS. Figure 9 inset also shows that the onset of water oxidation shifts to lower potential as the surface was heated to higher temperature and Ni diffused into the subsurface region. The highest current density (4.9 mA/cm^2 at 0.8 $V_{Ag/AgCl}$) was obtained on a Ni-incorporated surface that had been heated to 700 K (purple curve).

By comparing results from different surfaces, these electrochemical measurements validate our proposed picture of structural changes. Ni atoms are deposited on the surface and form clusters of mostly Ni(0). Then, annealing to 700 K leads to interdiffusion and incorporation of Ni into the near-surface region. Furthermore, these measurements of the onset potential shift and current density enhancement induced by Ni deposition and subsequent annealing are consistent with the theoretical prediction that Ni-incorporation into α-Fe_2O_3(0001) facilitates water oxidation.

CONCLUSION

Investigations by STM, LEED, XPS, and LEIS showed that incorporating Ni into the subsurface region of α-Fe_2O_3(0001) (hematite) by thermal annealing submonolayer deposits of Ni in vacuum to 700 K produced a Ni-free surface layer and changed the structure of the surface. Ni incorporation is associated with diffusion of Ni into the subsurface and the formation of FeO–like domains on the topmost layer. The Ni-incorporated α-Fe_2O_3(0001) surface was shown to stabilize surface-bound OH compared to that on the clean α-Fe_2O_3(0001) surface. These results are discussed in the context of a proposed water oxidation mechanism on this surface in which Ni doping facilitates water oxidation by increasing O hole concentrations and forms less negatively charged O anions

dx.doi.org/10.1021/am5062773 | ACS Appl. Mater. Interfaces 2014, 6, 22289–22296

(*O) and *O···OH species.[16] Electrochemical testing of the water oxidation performance was also carried out on these α-Fe_2O_3(0001) and the Ni-incorporated surfaces. The Ni-modified surfaces exhibited higher current density and lower onset potential for OER, a significant improvement over the unmodified α-Fe_2O_3(0001), consistent with these theoretical predictions.

■ ASSOCIATED CONTENT

Supporting Information

H_2O TPD on FeO(111) surface, LEIS and XPS depth profile of Ni-incorporated surface, and comparison of UPS on clean and Ni-incorporated α-Fe_2O_3(0001) surface without H_2O. This material is available free of charge via the Internet at http://pubs.acs.org.

■ AUTHOR INFORMATION

Corresponding Author

*E-mail: bkoel@princeton.edu.

Notes

The authors declare no competing financial interest.

■ ACKNOWLEDGMENTS

This work was supported by the Addy/ISN North American Low Carbon Emission Energy Self-Sufficiency Fund of the Andlinger Center for Energy and the Environment (ACEE) at Princeton University. The authors thank C. X. Kronawitter for helpful discussions and a critical reading of the manuscript.

■ REFERENCES

(1) Gao, H. W.; Liu, C.; Jeong, H. E.; Yang, P. D. Plasmon-Enhanced Photocatalytic Activity of Iron Oxide on Gold Nanopillars. *ACS Nano* **2012**, *6*, 234−240.

(2) Sivula, K.; Le Formal, F.; Gratzel, M. Solar Water Splitting: Progress Using Hematite(α-Fe_2O_3) Photoelectrodes. *ChemSusChem* **2011**, *4*, 432−449.

(3) Lin, Y. J.; Yuan, G. B.; Sheehan, S.; Zhou, S.; Wang, D. W. Hematite-Based Solar Water Splitting: Challenges and Opportunities. *Energy Environ. Sci.* **2011**, *4*, 4862−4869.

(4) Hahn, N. T.; Ye, H. C.; Flaherty, D. W.; Bard, A. J.; Mullins, C. B. Reactive Ballistic Deposition of α-Fe_2O_3 Thin Films for Photoelectrochemical Water Oxidation. *ACS Nano* **2010**, *4*, 1977−1986.

(5) Cesar, I.; Sivula, K.; Kay, A.; Zboril, R.; Graetzel, M. Influence of Feature Size, Film Thickness, and Silicon Doping on the Performance of Nanostructured Hematite Photoanodes for Solar Water Splitting. *J. Phys. Chem. C* **2009**, *113*, 772−782.

(6) Sanchez, C.; Sieber, K. D.; Somorjai, G. A. The Photoelectrochemistry of Niobium Doped α-Fe_2O_3. *J. Electroanal. Chem.* **1988**, *252*, 269−290.

(7) Zhao, P.; Kronawitter, C. X.; Yang, X. F.; Fu, J.; Koel, B. E. WO_3-α-Fe_2O_3 Composite Photoelectrodes with Low Onset Potential for Solar Water Oxidation. *Phys. Chem. Chem. Phys.* **2014**, *16*, 1327−1332.

(8) Liu, Y.; Yu, Y. X.; Zhang, W. D. Photoelectrochemical Properties of Ni-Doped Fe_2O_3 Thin Films Prepared by Electrodeposition. *Electrochim. Acta* **2012**, *59*, 121−127.

(9) Kleiman-Shwarsctein, A.; Hu, Y. S.; Forman, A. J.; Stucky, G. D.; McFarland, E. W. Electrodeposition of α-Fe_2O_3 Doped with Mo or Cr as Photoanodes for Photocatalytic Water Splitting. *J. Phys. Chem. C* **2008**, *112*, 15900−15907.

(10) Hu, Y. S.; Kleiman-Shwarsctein, A.; Forman, A. J.; Hazen, D.; Park, J. N.; McFarland, E. W. Pt-Doped α-Fe_2O_3 Thin Films Active for Photoelectrochemical Water Splitting. *Chem. Mater.* **2008**, *20*, 3803−3805.

(11) Kay, A.; Cesar, I.; Gratzel, M. New Benchmark for Water Photooxidation by Nanostructured α-Fe_2O_3 Films. *J. Am. Chem. Soc.* **2006**, *128*, 15714−15721.

(12) Jones, F.; Rohl, A. L.; Farrow, J. B.; van Bronswijk, W. Molecular Modeling of Water Adsorption on Hematite. *Phys. Chem. Chem. Phys.* **2000**, *2*, 3209−3216.

(13) Parker, S. C.; de Leeuw, N. H.; Redfern, S. E. Atomistic Simulation of Oxide Surfaces and Their Reactivity with Water. *Faraday Discuss.* **1999**, *114*, 381−393.

(14) Man, I. C.; Su, H. Y.; Calle-Vallejo, F.; Hansen, H. A.; Martinez, J. I.; Inoglu, N. G.; Kitchin, J.; Jaramillo, T. F.; Norskov, J. K.; Rossmeisl, J. Universality in Oxygen Evolution Electrocatalysis on Oxide Surfaces. *ChemCatChem* **2011**, *3*, 1159−1165.

(15) Yin, S. X.; Ellis, D. E. H_2O Adsorption and Dissociation on Defective Hematite(0001) Surfaces: A DFF Study. *Surf. Sci.* **2008**, *602*, 2047−2054.

(16) Liao, P. L.; Keith, J. A.; Carter, E. A. Water Oxidation on Pure and Doped Hematite(0001) Surfaces: Prediction of Co and Ni as Effective Dopants for Electrocatalysis. *J. Am. Chem. Soc.* **2012**, *134*, 13296−13309.

(17) Cheng, W. R.; He, J. F.; Sun, Z. H.; Peng, Y. H.; Yao, T.; Liu, Q. H.; Jiang, Y.; Hu, F. C.; Xie, Z.; He, B.; Wei, S. Q. Ni-Doped Overlayer Hematite Nanotube: A Highly Photoactive Architecture for Utilization of Visible Light. *J. Phys. Chem. C* **2012**, *116*, 24060−24067.

(18) Weiss, W.; Ranke, W. Surface Chemistry and Catalysis on Well-Defined Epitaxial Iron-Oxide Layers. *Prog. Surf. Sci.* **2002**, *70*, 1−151.

(19) Shaikhutdinov, S. K.; Weiss, W. Oxygen Pressure Dependence of the α-Fe_2O_3(0001) Surface Structure. *Surf. Sci.* **1999**, *432*, L627−L634.

(20) Shaikhutdinov, S. K.; Joseph, Y.; Kuhrs, C.; Ranke, W.; Weiss, W. Structure and Reactivity of Iron Oxide Surfaces. *Faraday Discuss.* **1999**, *114*, 363−380.

(21) Tang, Y. Y.; Qin, H. J.; Wu, K. H.; Guo, Q. L.; Guo, J. D. The Reduction and Oxidation of Fe_2O_3(0001) Surface Investigated by Scanning Tunneling Microscopy. *Surf. Sci.* **2013**, *609*, 67−72.

(22) Condon, N. G.; Leibsle, F. M.; Lennie, A. R.; Murray, P. W.; Vaughan, D. J.; Thornton, G. Biphase Ordering of Iron-Oxide Surfaces. *Phys. Rev. Lett.* **1995**, *75*, 1961−1964.

(23) Hendewerk, M.; Salmeron, M.; Somorjai, G. A. Water Adsorption on the(001) Plane of Fe_2O_3 - an XPS, UPS, Auger, and TPD Study. *Surf. Sci.* **1986**, *172*, 544−556.

(24) Mckay, J. M.; Henrich, V. E. Surface Electronic Structure of NiO: Defect States, O_2 and H_2O Interactions. *Phys. Rev. B* **1985**, *32*, 6764−6772.

(25) Fleisch, T.; Winograd, N.; Delgass, W. N. Chemisorption of Oxygen on Ni(100) by SIMS and XPS. *Surf. Sci.* **1978**, *78*, 141−158.

(26) Barbieri, A.; Weiss, W.; Vanhove, M. A.; Somorjai, G. A. Magnetite Fe_3O_4(111): Surface Structure by LEED Crystallography and Energetics. *Surf. Sci.* **1994**, *302*, 259−279.

(27) Lad, R. J.; Henrich, V. E. Structure of α-Fe_2O_3 Single-Crystal Surfaces Following Ar^+ Ion-Bombardment and Annealing in O_2. *Surf. Sci.* **1988**, *193*, 81−93.

(28) Bauer, E. Multiple Scattering Versus Superstructures in Low Energy Electron Diffraction. *Surf. Sci.* **1967**, *7*, 351−&.

(29) Carley, A. F.; Rassias, S.; Roberts, M. W. The Specificity of Surface Oxygen in the Activation of Adsorbed Water at Metal Surfaces. *Surf. Sci.* **1983**, *135*, 35−51.

(30) Norton, P. R.; Tapping, R. L.; Goodale, J. W. Photoemission Study of Interaction of Ni(100), Ni(110), and Ni(111) Surfaces with Oxygen. *Surf. Sci.* **1977**, *65*, 13−36.